Isolating excitonic Raman coherence in semiconductors using two-dimensional correlation spectroscopy

Lijun Yang,[1] Tianhao Zhang,[2,3] Alan D. Bristow,[2] Steven T. Cundiff,[2] and Shaul Mukamel[1,a)]
[1]*Department of Chemistry, University of California, Irvine, California 62697-2025, USA*
[2]*JILA, University of Colorado and National Institute of Standard & Technology, Boulder, Colorado 80309-0440, USA*
[3]*Department of Physics, University of Colorado, Boulder, Colorado 80309-0390, USA*

(Received 7 July 2008; accepted 28 October 2008; published online 19 December 2008)

We present the experimental and simulation results of two-dimensional optical coherent correlation spectroscopy signals along the phase-matching direction $\mathbf{k_I}=-\mathbf{k}_1+\mathbf{k}_2+\mathbf{k}_3$ projected on the two-dimensional (2D) (Ω_3,Ω_2) plane corresponding to the second and third delay periods. Overlapping Raman coherences in the conventional (Ω_3,Ω_1) 2D projection may now be clearly resolved. The linewidths of the heavy-hole (HH) and light-hole (LH) excitonic Raman coherence peaks are obtained. Further insights on the higher-order (beyond time-dependent Hartree–Fock) correlation effects among mixed (HH and LH) two excitons can be gained by using a cocircular pulse polarization configuration. © *2008 American Institute of Physics*. [DOI: 10.1063/1.3037217]

I. INTRODUCTION

Ultrafast spectroscopy has been extensively used to study the dynamic processes in molecules[1] and semiconductors.[2] Transient absorption reveals that energy relaxation and transient four-wave mixing (TFWM), also known as photon-echo spectroscopy, probe dephasing processes.

Recently, these studies have been extended by implementing ideas originally developed in nuclear magnetic resonance.[3] These techniques require that the phase of the emitted field be measured as a function of delay between the excitation pulses, which itself must have subwavelength stability. Correlations between resonances can be determined by taking a two-dimensional Fourier transform with respect to the emission time and the delay between excitation pulses. This family of techniques, known as multidimensional correlation spectroscopy[4–6] or multidimensional Fourier transform spectroscopy, is typically implemented using a three-pulse TFWM geometry. Consequently, there are three time delays, the delay between the first two pulses t_1, the delay between the second and third pulses t_2, and the emission time after the third pulse t_3. Fourier transforming with respect to all three of these to obtain corresponding frequency variables, Ω_1, Ω_2, and Ω_3, would yield a three-dimensional spectrum. Two-dimensional (2D) spectra are obtained by holding one time delay fixed. 2D correlation spectroscopy (2DCS) has clarified numerous subtleties of dynamics and coherences inaccessible by conventional TFWM.

Coherent one-dimensional (1D) optical spectroscopy has been extensively used to study excitation dynamics in direct gap semiconductors, such as GaAs.[7] The optical properties near the fundamental gap at low temperature are dominated by excitonic (bound electron-hole pair) resonances. While the original goal was to study dynamics, it quickly became clear that the coherent response was dominated by many-body effects, particularly for the excitonic resonances. These effects were classified phenomenologically as local field,[8] excitation induced dephasing,[9] biexcitonic,[10] or excitation induced shift.[11] Modeling these phenomena requires going beyond the Hartree–Fock approximation used in the semiconductor Bloch equations,[12] thus higher order terms must be included using the nonlinear exciton equations (dynamics controlled truncation).[13,14] Coupling between excitonic and continuum states was also shown to dramatically influence the coherent response.[15] Despite the good agreement between experiment and theory, it was difficult to separate the various contributions using traditional coherent spectroscopic techniques.

Over the past few years, 2DCS has greatly enhanced the understanding of many-body effects in the coherent response of semiconductor quantum wells (QWs). Initial results showed the dominance of many-body effects and coupling to the continuum.[16] Insight into the phenomenological description of many-body effects was gained by examining the lineshapes[17] and the polarization dependence.[18] In parallel, theoretical descriptions of 2DCS signals from semiconductors have been developed.[19–21] 2DCS has also recently been applied to semiconductor quantum dots.[22] In these studies, a 2D spectrum was obtained by detecting the signal in the direction $\mathbf{k_I}=-\mathbf{k}_1+\mathbf{k}_2+\mathbf{k}_3$ and holding the delay between the second and third pulses fixed. We designate such spectra as $S_{\mathrm{I}}(\Omega_3,t_2,\Omega_1)$.

Raman coherences between two states not directly coupled by a transition dipole are of interest for the study of coherent processes in semiconductors[23,24] as well as in photosynthetic[25] complexes. It is also essential for effects such as electromagnetically induced transparency, lasing without inversion and slow light.[26] The Raman coherence among heavy-hole (HH) and light-hole (LH) excitons can produce quantum beats in TFWM experiments. However, early experiments on quantum beats in QWs and in bulk

a)Electronic mail: smukamel@uci.edu.

semiconductors[27,28] cannot easily isolate or are very insensitive to the Raman coherence. In fact, standard two-pulse TFWM experiments are not able to determine the dephasing rate of the Raman coherence between HH and LH excitons due to their limitations (see details in Sec. II).[28–33] This is due to the fact that this coherence intrinsically overlaps with many other contributions such as ground state bleaching, inhomogeneous broadening, and the polarization interference (PI) from localized excitons.[34–36] The correlation of the inhomogeneity may also affect the investigation of Raman coherence.[37] Furthermore, Raman coherence is overlapped with optical coherence in conventional two-pulse or three-pulse TFWM experiments. Early measurement of Raman coherence between HH and LH excitons in semiconductors was measured by observing oscillations in a transient absorption experiment.[29] Further work revealed the essential role of exciton-exciton interactions in the signal.[38] Evidence for intervalence band coherences were also found by using the optical Stark effect.[33] Recently, three-pulse TFWM was used to simultaneously measure the dephasing of both the Raman and optical coherences, which allows the correlation coefficient for the dephasing processes to be determined.[39]

The 2D correlation spectra that employ S_I (photon echo) show photon-echo signals when displayed as 2D (Ω_3,Ω_1) spectra for various values of t_2. In this work, we show that a different projection, (Ω_3,Ω_2) for a fixed t_1, provides interesting new information. $S_I(\Omega_3,\Omega_2,t_1)$ is obtained by a double Fourier transform with respect to t_3 and t_2 with the corresponding conjugate frequencies Ω_3 and Ω_2, holding t_1 fixed.[19] This signal can reveal Raman coherences[29,33,38] and other many-body correlations unavailable in the traditional $S_I(\Omega_3,t_2,\Omega_1)$ signal. The two projections thus carry complementary information.

II. BASIC PRINCIPLES OF 2D SIGNALS

The 2D correlation spectra show peaks that correspond to pathways in a third-order perturbation calculation of the system density matrix. Double-sided Feynman diagrams[1,40] are a convenient tool for describing and cataloging these resonances within the rotating wave approximation.

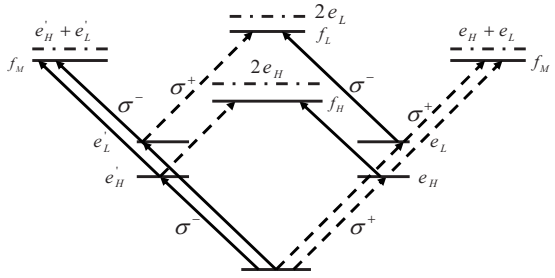

FIG. 1. Level scheme of the complete single- and two-exciton transitions for a semiconductor QW.

GaAs has a single conduction band (CB) and two valence bands for HH and LH holes. In bulk GaAs, these two bands are degenerate at $\mathbf{k}=0$. Quantum confinement lifts the degeneracy. Exciton resonances occur for transitions between the HH and CB and between the LH and CB. These two resonances are well resolved for QW thicknesses around 10 nm. The level scheme of the HH and LH excitons is shown in Fig. 1. The HH and LH excitons are denoted by e_H and e_L, respectively, in the diagrams. The diagram also shows the possible two-exciton states, including pure HH (LH) and mixed (HH+LH) two excitons. These are denoted, respectively, as f_H (f_L) and f_M. Right and left circularly polarized light are denoted as σ^+ and σ^-, respectively.

A. Feynman diagrams and the corresponding expressions for the S_I technique

Three basic Feynman diagrams contribute to the S_I signal. These are associated with (i) ground-state bleaching (GSB), (ii) excited-state emission (ESE), and (iii) excited-state absorption (ESA).[6,19] The complete set of diagrams is shown in Fig. 2. These are all derived from the three basic diagrams by including all contributions of the HH and LH

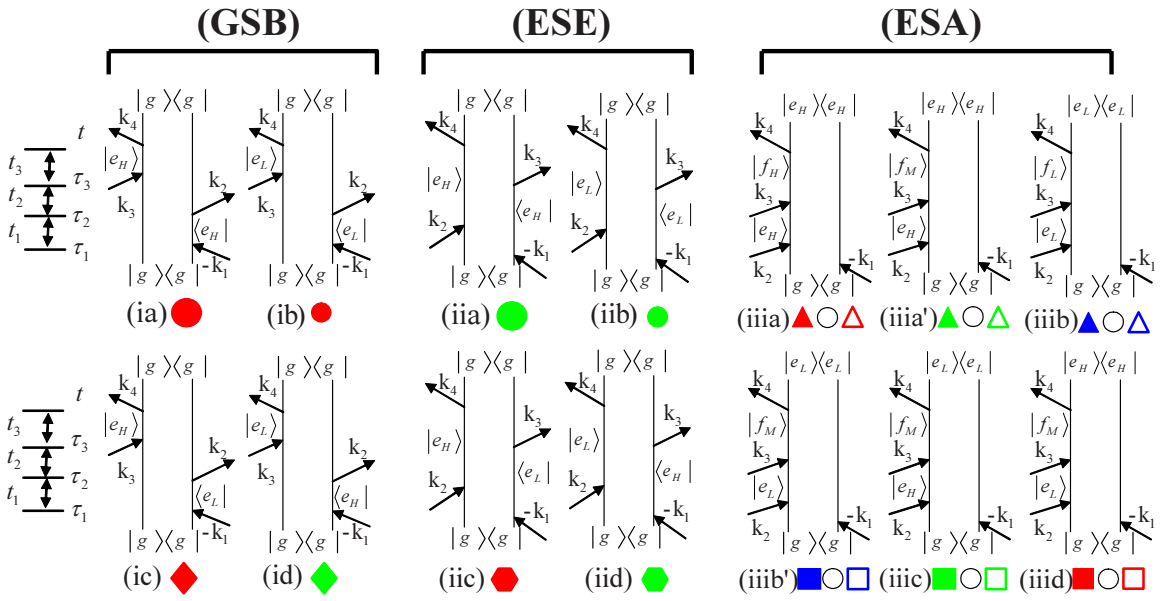

FIG. 2. (Color online) Feynman diagrams for S_I technique.

exciton transitions.[19] As in Fig. 1, the HH and LH excitons are denoted e_H and e_L, respectively. Different symbols below each diagram represent that diagram on the schematic representations of 2DCS in Secs. II B and II C. Contributions from the GSB and ESE diagrams are labeled with red and green symbols. The colored circles pertain to pathways that include solely e_H or e_L processes, whereas the diamonds and hexagons represent pathways containing both e_H or e_L transition. For the ESA pathways, the three symbols are shown for each diagram. The open circles appearing in each diagram represent the contributions from either pure or mixed two-exciton states within time-dependent Hartree–Fock (TDHF) approximation, where no energy shifts exist from correlation effects. Two-exciton contributions coming from going beyond the TDHF approximation are denoted by colored triangles and squares, where the solid (open) symbols describe redshifted (blueshifted) two-exciton states. Note that, for simplicity, we have extended the conventional naming of ESE to include the diagrams without diagonal element in the t_2 period (e.g., iic and iid) because all these diagrams are derived from the same type of pathway. The same is for ESA.

The sum-over-state expression[1,19] for the response functions, $R_I^{(3)}$, which corresponds to the diagrams in Fig. 2,

$$R_{\mathrm{I}}^{(3)}(t_3,t_2,t_1) = i^3\sum_{e,e'}(\mathbf{e}_1\cdot\mu_{ge'})(\mathbf{e}_2\cdot\mu_{e'g})(\mathbf{e}_4\cdot\mu_{ge})(\mathbf{e}_3\cdot\mu_{eg})e^{-(i\omega_{eg}+\Gamma_{eg})t_3-\Gamma_{gg}t_2+(i\omega_{e'g}-\Gamma_{e'g})t_1} + i^3\sum_{e,e'}(\mathbf{e}_1\cdot\mu_{ge'})(\mathbf{e}_3\cdot\mu_{e'g})(\mathbf{e}_4\cdot\mu_{ge})$$
$$\times(\mathbf{e}_2\cdot\mu_{eg})e^{-(i\omega_{eg}+\Gamma_{eg})t_3-(i\omega_{ee'}+\Gamma_{ee'})t_2+(i\omega_{e'g}-\Gamma_{e'g})t_1} - i^3\sum_{e,e',f}(\mathbf{e}_1\cdot\mu_{ge'})(\mathbf{e}_4\cdot\mu_{e'f})(\mathbf{e}_3\cdot\mu_{fe})$$
$$\times(\mathbf{e}_2\cdot\mu_{eg})e^{-(i\omega_{fe'}+\Gamma_{fe'})t_3-(i\omega_{ee'}+\Gamma_{ee'})t_2+(i\omega_{e'g}-\Gamma_{e'g})t_1}, \quad (1)$$

where both e and e' can be either e_H and e_L; $\omega_{vv'}=\varepsilon_v-\varepsilon_{v'}$ $(v,v'=g,e,e',f=f_H,f_L,$ or $f_M)$ is the frequency and $\Gamma_{vv'}$ are the dephasing rate of the $v\rightarrow v'$ transition. $\mathbf{e}_i$ $(i=1,2,3,4)$ are the unit polarization vector of the three pulses and the fourth heterodyne pulse. $\mu_{vv'}$ are the transition dipoles for various resonances. From Eq. (1), it can be seen that Raman coherences $(\propto e^{-i\omega_{ee'}t_2})$ occur only in the second and third terms when $e\neq e'$ and are related to the time delay t_2 (the delay between second and third pulses). The Raman coherence corresponds to diagrams (iic), (iid), (iiic), and (iiid) in Fig. 2. The dephasing rates for Raman coherence and optical coherence are, respectively, given by $\Gamma_{ee'}$ $(e\neq e')$ and $\Gamma_{e'g}$. From Eq. (1), it can be seen that it is desirable to measure the Raman coherence and its dephasing along t_2 or its frequency counterpart, Ω_2. However, early experiment[27] on quantum beats among LH and HH excitons was performed along the time delay t_1 (the delay between the first and second pulses) in a two-pulse scheme TFWM at positive time delays. Thus the beats in these type of experiments should be dominated by the PI from localized excitons. At negative delays, although the TFWM signal varies as a function of t_2, the signal itself is no longer photon echo anymore. Instead, the negative-delay signal for a two-pulse scheme TFWM (Ref. 27) corresponds to double-quantum coherence signals[41] where we can see the exciton-biexciton beats rather than the quantum beats induced by Raman coherence.

The Feynman diagrams and the corresponding expressions given above are used to qualitatively analyze various pathways appearing in different projections of the spectrum in GaAs QWs. This analysis can provide significant insights to the 2D spectra obtained from numerical simulations in Sec. IV. However, there is no one-to-one mapping between the diagrams and our numerical calculations. Though it is tempting to reason that the Raman coherence diagrams (iic), (iid), (iiic), and (iiid) could cancel if we assume that exciton-to-two-exciton and ground-state-to-single-exciton transition dipoles (and frequencies) are close to each other, we will find that this is not the case in our experiments and numerical simulations. This suggests that the assumptions above are not good for semiconductors. A reasonable argument is that the single-exciton contribution from (iic) and (iid) are much stronger than that of (iiic) and (iiid). This is due to the fact that the dynamics of (iiic) and (iiid) involves two-exciton transitions.

B. Photon-echo signals in the (Ω_3,Ω_1) projection plane

The peak pattern of different contributions to the conventional $S_{\mathrm{I}}(\Omega_3,t_2,\Omega_1)$ spectrum is displayed in Fig. 3. Fig-

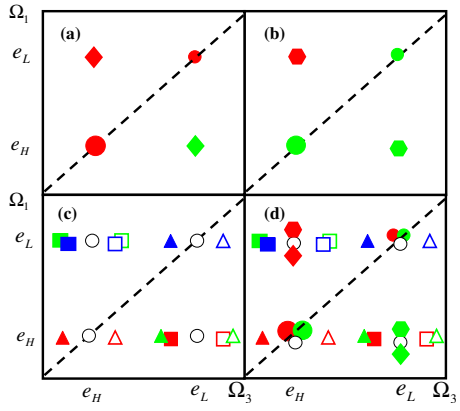

FIG. 3. (Color online) Schematic $S_{\mathrm{I}}(\Omega_3,t_2,\Omega_1)$ spectra for the various contributions derived from Fig. 2. Panel comprises the (a) GSB diagrams (ia)–(id), panel (b) the ESE diagrams (iia)–(iid), panel (c) ESA diagrams (iiia)–(iiid), and panel (d) shows the total spectrum.

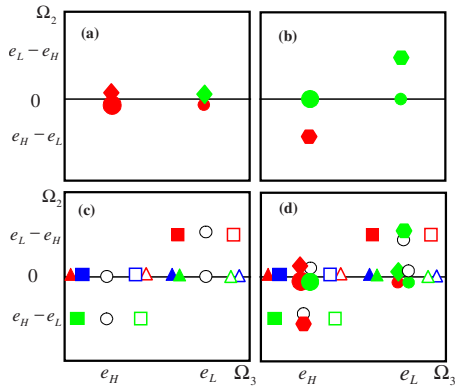

FIG. 4. (Color online) Schematic $S_I(\Omega_3,\Omega_2,t_1)$ spectra for the various contributions derived from Fig. 2. Panel comprises the (a) GSB diagrams (ia)–(id), panel (b) the ESE diagrams (iia)–(iid), panel (c) ESA diagrams (iiia) to (iiid), and panel (d) shows the total spectrum.

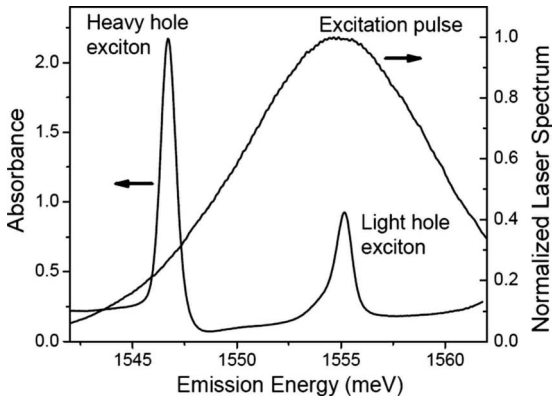

FIG. 5. Experimental linear absorption and pulse power spectrum.

ures 3(a) and 3(b) show, respectively, the GSB, ESE, and ESA of Fig. 2, and Fig. 3(d) is the total spectrum. For GSB and ESE cases, a single diagram contributes to each of the diagonal and off-diagonal peaks of the 2D spectrum. For the ESA there are several contributions per diagram. Only the TDHF component of the diagrams contributes to the center position of each of the diagonal and off-diagonal peaks. The diagonal peaks have one contribution each to the red- and blueshifted sides of the peak, related to correlated pure two-exciton pathways. The red- and blueshifted off-diagonal peaks are from the mixed two-exciton pathways. The overlapping symbols have been slightly displaced for clarity.

C. Photon-echo signals in the (Ω_3,Ω_2) projection plane

The $S_I(\Omega_3,\Omega_2,t_1)$ spectra are sketched in Fig. 4 where the four panels, respectively, show the GSB, ESE, and ESA contributions and the total spectrum [Fig. 4(d)]. The vertical axis is associated with the mixing time t_2 and shows most contributions near zero frequency. In Fig. 4(a), all the GSB contributions are seen along the zero mixing frequency position ($\Omega_2=0$). In Fig. 3, these were distributed into diagonal and off-diagonal components. For Fig. 4(b), the ESE contributions appear at different positions, where the off-zero peaks are related to the Raman coherence between HH and LH excitons. The red hexagon associated with the HH emission is at $(\Omega_3,\Omega_2)=(e_H,e_H-e_L)$ and the green hexagon associated with the LH emission is at $(\Omega_3,\Omega_2)=(e_L,e_L-e_H)$. Similarly in Fig. 4(c), the ESA (or two-exciton) resonances are well separated.

This projection allows for clearer observation of the Raman coherence. In the (Ω_3,Ω_1) projection plane, the ESE and GSB peaks overlap (red and green diamonds shown in Fig. 3) and may not be resolved. In the total spectrum of the (Ω_3,Ω_2) projection [Fig. 4(d)], two types of contributions to Raman coherence, (iic) and (iid) and (iiic) and (iiid), overlap at $\Omega_2\neq 0$. These two contributions are, respectively, positive and negative and thus reduces the overall strength of observed peaks at these positions. In QWs, however, the contribution from two excitons are generally weak as compared to the single-exciton counterpart. Thus experimentally we still can observe Raman coherence.

Different 2D projections provide complementary information by separating various types of peaks in a different way. Not all the contributions represented by Feynman diagrams can be clearly resolved in a single 2D spectrum due to their different relative strength obtained with different excitation conditions and pulse polarization configurations. For example, the beyond TDHF contributions in Figs. 3 and 4 cannot be easily seen in the present $S_I(\Omega_3,\Omega_2,t_1)$ but can be easily resolved in other 2D techniques such as double-quantum coherence 2DCS $S_{III}(\Omega_3,\Omega_2,t_1)$[41] or in $S_I(\Omega_3,t_2,\Omega_1)$.[19,20] In $S_I(\Omega_3,\Omega_2,t_1)$, however, Raman coherence is isolated from many other contributions. GSB contribution is completely isolated from Raman coherence because it appears at $\Omega_2=0$. The effect of localized excitons should also be significantly suppressed. If the PI arises from the interference of HH and LH excitons localized in different regions of a QW, then they can be treated as uncoupled two-level systems.[34–36] In this case, PI will not overlap with Raman coherence because uncoupled two-level system will contribute only to the region of $\Omega_2=0$ in $S_I(\Omega_3,\Omega_2,t_1)$. However, if both HH and LH excitons are localized in the same site of a QW, then these localized excitons will contribute to the Raman coherence. Inhomogeneous broadening of localized excitons should affect the width of the measured Raman coherence.

In Sec. III, we study the separation of Raman coherences in the (Ω_3,Ω_2) projection plane experimentally and numerically.

III. EXPERIMENTS

The multiple QW sample employed in the experiments consists of ten periods $GaAs/Al_{0.3}Ga_{0.7}As$ with 10 nm wells and 10 nm barriers, grown by molecular beam epitaxy. The sample temperature is kept below 10 K in a cold-finger cryostat. The absorption spectrum displays the prominent HH and LH exciton resonances with an energy splitting 8.4 meV, as shown in Fig. 5. The incident pulses have sufficient bandwidth to excite both HH and LH exciton resonances.

The 2D experimental geometry is shown in Fig. 6. The laser source is a mode-locked 100 fs Ti:sapphire laser, which

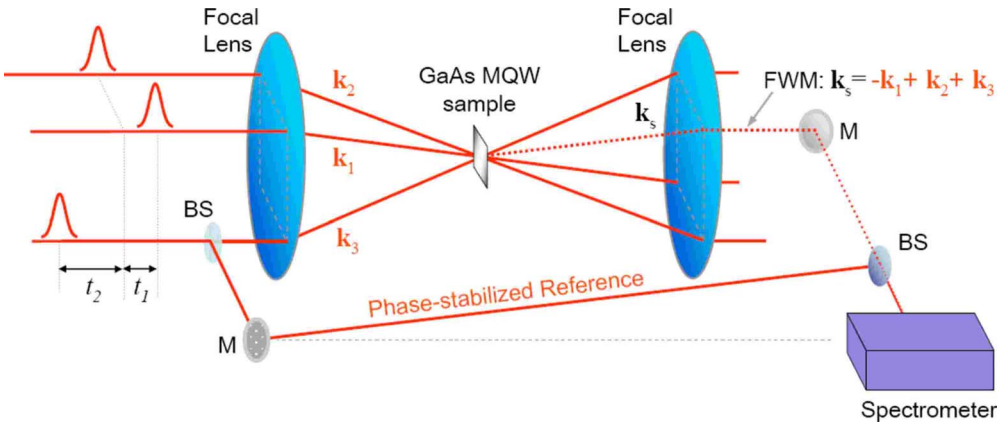

FIG. 6. (Color online) Experimental setup.

has a repetition rate of 76 MHz and a tunable wavelength around 800 nm. The laser is tuned to a photon energy of 1.555 eV, so that it centered over the LH exciton to compensate for its weaker oscillator strength. The laser pulses are split into four identical pulses and arranged in the standard box geometry. Three of the pulses are used to generate a TFWM experiment, while the fourth beam traces out the direction of the TFWM emission. The fourth beam is used for alignment and is blocked during acquisition of the spectra. The wave vectors of the excitation beams are $\mathbf{k}_1$, $\mathbf{k}_2$, and $\mathbf{k}_3$ propagating from three corners of the square to the QW sample, after being focused by a single 20 cm focal length lens. The TFWM signal is emitted in the phase-matched direction $-\mathbf{k}_1+\mathbf{k}_2+\mathbf{k}_3$ and is collimated by another 20 cm focal length lens. The emission is combined on a beam splitter with a reference beam that is split from the third beam before the sample and routed around the cryostat. The combined signal and reference are coupled into a single-mode fiber and transmitted to a spectrometer. The resulting spectral interferogram is recorded with a charge-coupled device camera so as to retrieve the complex TFWM spectrum.[42]

The 2D data are acquired by recording a series of interferograms as a function of delay t_2, which is scanned with a step size of 26.67 fs with a translation stage. The delay t_1 is set to 0 and actively stabilized by a servo loop. The phase of the reference relative to the third pulse is also actively stabilized.[43] The 2D spectrum, $S_I(\Omega_3,\Omega_2,t_1)$, is the result of Fourier transforming $S_I(t_3,t_2,t_1)$ with respect to t_2 and t_3. The Fourier transform with respect to t_3 is provided by the spectrometer and the Fourier transform with respect to t_2 is performed numerically.

In Figs. 7(a) and 7(b), we present the two experimental 2D spectra obtained, respectively, with collinear and cocircular polarized excitation pulses. The spectra are normalized according to the strongest peak. However, to clearly extract the relatively weak Raman coherence, we display the amplitude 2D spectra from zero to 0.1. In the collinear case [Fig. 7(a)], there are two separated peaks away from zero mixing energy ($\Omega_2=0$). These two peaks, denoted (a) and (b), correspond, respectively, to the red and green hexagons (Raman coherences) in Fig. 4(d). They are the only two peaks we are interested in this work. Other peaks at $\Omega_2 \neq 0$ are attributed to either continuum states of HH or LH excitons or possible disorder in QWs; many of these peaks are weak even compared to the Raman coherences. Both the Raman coherences and the continuum states are visible due to "windowing" of the time series before performing the Fourier transform.[3] This is required since the population lifetime of semiconductor QWs is much longer than both the typical dephasing times and the practical length of the t_2 scanning range. Hence, truncating the long lifetime signal leads to a step function in the time series, which when transformed produces ripples in the form of a sinc(ω) function and thus compromising resolution. The applied Hanning window ($h(t)=0.5+0.5\cos(\pi t/t_{\max})$) is appropriately chosen to remove ripples without unduly broadening the linewidths in the transform direction; here we use $t/t_{\max}=0.6$.

It should be emphasized that the extraction of Raman coherence from $S_I(\Omega_3,\Omega_2,t_1)$ is at the expense of the resolution of other contributions to the signals. For example, while the two strong contributions involving only single excitons, red diamond and red circle, do not overlap in $S_I(\Omega_3,t_2,\Omega_1)$ [Fig. 3(d)], they are completely overlapped in $S_I(\Omega_3,\Omega_2,t_1)$ at $\Omega_2=0$. These make the contributions at $\Omega_2=0$ very strong and almost no clear information can be derived from these strong peaks. However, Raman coherences can be easily resolved in the $S_I(\Omega_3,\Omega_2,t_1)$ and we can obtain their information. For example, we can easily extract their linewidth. In the collinear case of Fig. 7(a), we estimate that the linewidths of the two Raman coherences are $\gamma_{Rh}=3.4\pm0.03$ meV and $\gamma_{Rl}=1.8\pm0.08$ meV for the HH and LH excitons, respectively. We expect that these linewidths will be the same. The difference between them may be due relative alignment of truncation artifacts to the peaks. It may also be related to the relative amplitudes of the HH and LH peaks. The overall strength of the LH peaks is smaller than those for the HH exciton: the $\Omega_2=0$ frequency LH is ~14% the strength of the HH peak. Even though the overall amplitude of the LH Raman coherence peak is 25% weaker than the HH Raman coherence peak, the relative strengths are 4% and 19% for the HH and LH side peaks compared to the $\Omega_2=0$ frequency peaks.

The other interesting information that can be obtained from the $S_I(\Omega_3,\Omega_2,t_1)$ 2D projection is shown in the 2D spectrum with cocircular polarized excitation [Fig. 7(b)]. The

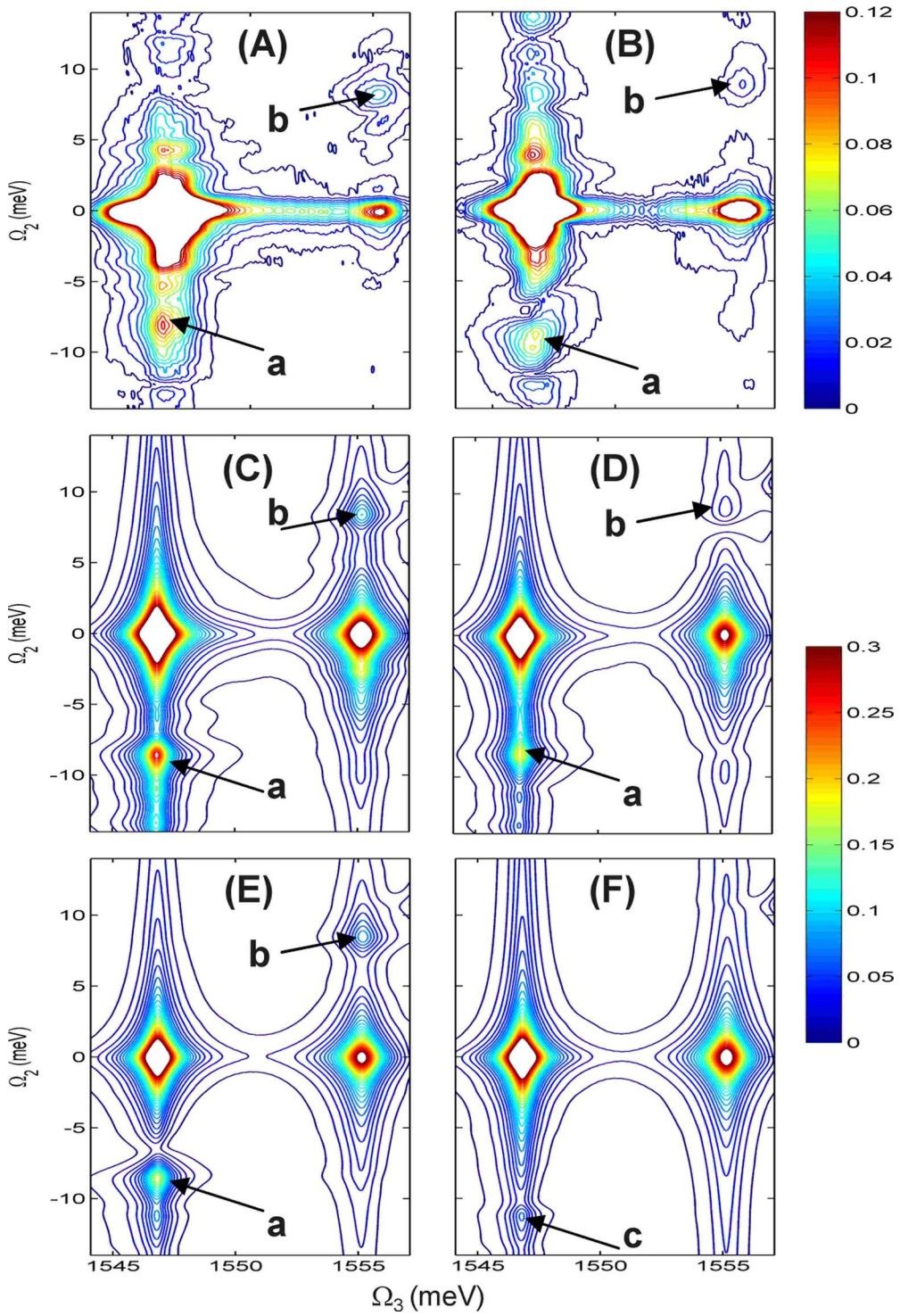

FIG. 7. (Color online) (Top) Experimental results with collinear excitation (left) and cocircular excitation (right). (Middle) Simulated 2D spectra with collinear (left) and cocircular excitations (right). (Bottom) Simulated 2D spectra with only TDHF contribution: (left) collinear excitations; (right) cocircular excitations. In each panel, the Raman coherence side peaks are denoted by (a) and (b) for emission at the HH and LH excitons, respectively.

amplitude of the Raman coherence side peaks, denoted (a) and (b), are smaller under these excitation conditions. As shown in the Appendix, these two peaks are induced by pure correlation effects beyond the TDHF approximation. This is due to the fact that, for cocircular excitations, there are no contributions within TDHF to peak positions (a) and (b) in Fig. 7(b) to third-order in the optical field. Thus the $S_I(\Omega_3,\Omega_2,t_1)$ projection provides a clear picture of beyond TDHF correlation effects among mixed two excitons.

IV. SIMULATIONS

We next present numerical simulations of these experiments based on a multiband 1D tight-binding Hamiltonian.[2,44,45] The Heisenberg equations of motion derived from this Hamiltonian are truncated according to the dynamics controlled truncation scheme.[13,14] This 1D tight-binding model includes HH and LH excitons and their continuum states in a tractable way and qualitatively account for

various features of 1D four-wave mixing[2] and 2DCS signal processes.[17,19,20,41] Parameters are chosen to fit the HH and LH exciton energies, oscillator strength, and energy splitting determined from the linear absorption spectrum. HH and LH excitons dominate the optical spectra with the chosen pulse center frequency and bandwidth. Some preliminary results on the role of continuum excitonic states on the 2DCS can be found in Refs. 16 and 18.

Figure 7(c) displays the simulated spectrum $S_I(\Omega_3,\Omega_2,t_1)$ for a collinear polarization configuration. Two Raman coherence peaks are denoted as (a) and (b) in the 2D spectra. Due to the limitation of the 1D tight-binding model, the calculated 2D spectrum is only qualitatively in agreement with the experimental results in Fig. 7(a). Figure 7(d) shows the calculated spectrum $S_I(\Omega_3,\Omega_2,t_1)$ for cocircular excitation. We find that the two side peaks, (a) and (b), are weaker as compared to their counterparts with collinear excitations in Fig. 7(c). This trend qualitatively agrees with the experiments with collinear and cocircular excitations [Figs. 7(a) and 7(b)].

Figures 7(e) and 7(f) show the signals calculated within the TDHF approximation.[19] There are still two side peaks, (a) and (b), corresponding to the Raman coherences for collinear excitations [Fig. 7(e)]. Thus, for the collinear excitation, HH and LH excitons are coupled even within the TDHF approximation. However, for cocircular excitations, the two side peaks are completely gone [Fig. 7(f)]. Note that the weak feature denoted (c) in Fig. 7(f) is from continuum states and is not a side peak from the HH and LH excitons. Thus we arrive at the conclusion that within TDHF approximation [Fig. 7(f)], there are no signatures of couplings among the LH and HH excitons to third order in the optical field with cocircular excitations. Any side peaks, such as peaks (a) and (b) in Fig. 7(d) with full calculation, are from pure correlation effects beyond TDHF. This is also the reason why the two side peaks (a) and (b) in the experiment with co circular excitations [Fig. 7(b)] are from pure correlation effects.

A. Separation of Raman coherences by narrow-bandwidth excitations

Raman coherences may also be separated by using narrow-bandwidth pulses that can selectively excite HH or LH excitons. This has been used to dissect photon-echo pathways and to achieve higher resolution of mixed two excitons in a double- quantum coherence technique.[46] Here we employ this technique to isolate the Raman coherence. We employ three narrow-bandwidth pulses that can, respectively, excite only LH, HH, and LH excitons. We thus select only pathways (iic) and (iiic) in Fig. 2. The corresponding schematic 2DCS is shown in the left panel of Fig. 8. Had we chosen another pulse sequence that can excite only HH, LH and HH excitons, then the other two pathways (iid) and (iiid) are selected and the corresponding schematic 2DCS is shown in the right panel of Fig. 8.

In Fig. 9, we present the simulated 2D spectra corresponding to the schematic representation in Fig. 8. Raman coherence is now completely separated from all other contributions.

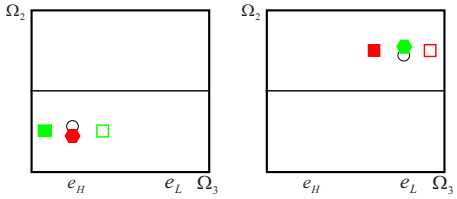

FIG. 8. (Color online) Schematic 2DCS corresponding to (left) a pulse sequence that excite only LH, HH, and LH excitons, respectively; (right) a pulse sequence that excite only HH, LH, and HH excitons, respectively.

V. CONCLUSIONS

We presented the experimental and simulation results of a 2D correlation spectroscopy technique that can isolate the Raman coherence between LH and HH excitons in semiconductor QWs. Such coherences, which overlap with other dominant single-exciton contribution in $S_I(\Omega_3,t_2,\Omega_1)$, may be resolved in the $S_I(\Omega_3,\Omega_2,t_1)$ signal. We also proposed a way to separate the Raman coherence in a background-free way.

ACKNOWLEDGMENTS

S.M. and S.T.C. gratefully acknowledge the support of the Chemical Sciences, Geosciences, and Biosciences Division, Office of Basic Energy Sciences, U.S. Department of Energy.

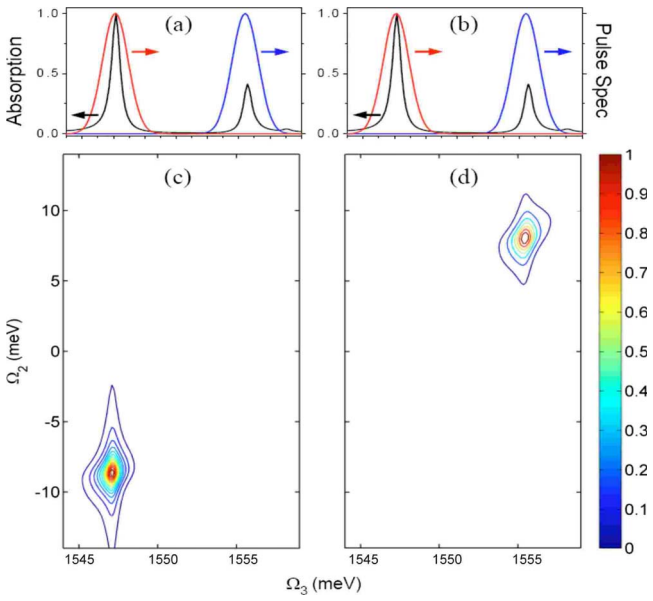

FIG. 9. (Color online) Simulated 2DCS with (left) a pulse sequence that can only excite LH, HH, and LH excitons, respectively; (right) a pulse sequence that can only excite HH, LH, and HH excitons, respectively. The pulse power spectra are shown on top of each 2D spectrum.

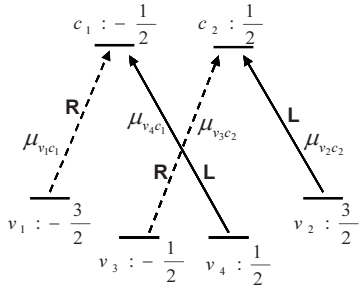

FIG. 10. Selection rules for HH and LH dipole transitions.

APPENDIX: COCIRCULAR POLARIZATION CONFIGURATION

To analyze the signals for cocircular polarization, we first present the optical selection rules for GaAs semiconductor QWs, which are represented by two conduction orbitals $J_z=\pm\frac{1}{2}$ and four valence orbitals, $J_z=\pm\frac{3}{2}$ (HH) and $J_z=\pm\frac{1}{2}$ (LH).[10,47–49] The dipole selection rules are presented in Fig. 10. The allowed transitions are denoted by R and L arrows, representing right and left circularly polarized photons, respectively. The corresponding transition dipoles are μ_{vc}, where $v=1,2$ denote HHs $\left(J_z=\pm\frac{3}{2}\right)$ and $v=3,4$ represent LHs $\left(J_z=\pm\frac{1}{2}\right)$. $c=1$ and 2 denote electrons with different spins in the CB $\left(J_z=\pm\frac{1}{2}\right)$.

R polarized photons can induce two transitions, (v_1,c_1) and (v_3,c_2). L polarized photons induce two other transitions, (v_2,c_2) and (v_4,c_1), as shown in Fig. 10. As shown in Ref. 50, the TDHF contribution is dominated by the term $\Sigma_{klv'c'}(p_{lk}^{v'c'})^* p_{lj}^{v'c} p_{ik}^{vc'}$ in the equations of motion. For S_I technique, we first consider the term $(p_{lk}^{v'c':\mathbf{k}_1})^* p_{lj}^{v'c:\mathbf{k}_2} p_{ik}^{vc':\mathbf{k}_3}$. For RRRR configuration, the indices (v',c') in $(p_{lk}^{v'c':\mathbf{k}_1})^*$ can be either (v_1,c_1) or (v_3,c_2) for the R polarized pulse $\mathbf{k}_1$, as shown in Fig. 10. For $(v',c')=(v_1,c_1)$, we have

$$\sum_{kl'c'} (p_{lk}^{v'c':\mathbf{k}_1})^* p_{lj}^{v'c:\mathbf{k}_2} p_{ik}^{vc':\mathbf{k}_3} = \sum_{kl} (p_{lk}^{v_1c_1:\mathbf{k}_1})^* p_{lj}^{v_1c:\mathbf{k}_2} p_{ik}^{vc_1:\mathbf{k}_3}. \tag{A1}$$

Since both $\mathbf{k}_2$ and $\mathbf{k}_3$ pulses are R polarized, the c and v indices in Eq. (A1) can only assume, respectively, the values $c=c_1$ and $v=v_1$. Thus this term cannot couple LH and HH excitons through cocircular excitation. The situation is the same when $(v',c')=(v_3,c_2)$. This is shown as follows:

$$\sum_{klv'c'} (p_{lk}^{v'c':\mathbf{k}_1})^* p_{lj}^{v'c:\mathbf{k}_2} p_{ik}^{vc':\mathbf{k}_3} = \sum_{kl} (p_{lk}^{v_3c_2:\mathbf{k}_1})^* p_{lj}^{v_3c:\mathbf{k}_2} p_{ik}^{vc_2:\mathbf{k}_3}. \tag{A2}$$

From similar analysis of the other term coming from the permutation among different wavevectors such as $\Sigma_{klv'c'}(p_{lk}^{v'c':\mathbf{k}_1})^* p_{lj}^{v'c:\mathbf{k}_3} p_{ik}^{vc':\mathbf{k}_2}$, we can obtain the same conclusion that cocircular excitations cannot couple LH and HH excitons.

[1] S. Mukamel, *Principles of Nonlinear Optical Spectroscopy* (Oxford University Press, New York, 1995).
[2] T. Meier, P. Thomas, and S. Koch, *Coherent Semiconductor Optics* (Springer-Verlag, Berlin, 2007).
[3] R. Ernst, G. Bodenhausen, and A. Wokaun, *Principles of Nuclear Magnetic Resonance in One and Two Dimensions* (Oxford Science, Oxford, 1987).
[4] V. Chernyak, W. M. Zhang, and S. Mukamel, J. Chem. Phys. **109**, 9587 (1998).
[5] W. M. Zhang, V. Chernyak, and S. Mukamel, J. Chem. Phys. **110**, 5011 (1999).
[6] S. Mukamel, Annu. Rev. Phys. Chem. **51**, 691 (2000).
[7] For a recent review, see S. T. Cundiff, Opt. Express **16**, 4639 (2008).
[8] K. Leo, M. Wegener, J. Shah, D. S. Chemla, E. O. Göbel, T. C. Damen, S. Schmitt-Rink, and W. Schäfer, Phys. Rev. Lett. **65**, 1340 (1990); M. Wegener, D. S. Chemla, S. Schmitt-Rink, and W. Schäfer, Phys. Rev. A **42**, 5675 (1990).
[9] H. L. Wang, K. Ferrio, D. G. Steel, Y. Z. Hu, R. Binder, and S. W. Koch, Phys. Rev. Lett. **71**, 1261 (1993); Y. Z. Hu, R. Binder, S. W. Koch, S. T. Cundiff, H. Wang, and D. G. Steel, Phys. Rev. B **49**, 14382 (1994).
[10] K. Bott, O. Heller, D. Bennhardt, S. T. Cundiff, P. Thomas, E. J. Mayer, G. O. Smith, R. Eccleston, J. Kuhl, and K. Ploog, Phys. Rev. B **48**, 17418 (1993).
[11] J. M. Shacklette and S. T. Cundiff, Phys. Rev. B **66**, 045309 (2002).
[12] S. Schmitt-Rink, D. S. Chemla, and D. A. B. Miller, Phys. Rev. B **32**, 6601 (1985); M. Lindberg and S. W. Koch, *ibid.* **38**, 3342 (1988).
[13] V. M. Axt and A. Stahl, Z. Phys. B: Condens. Matter **93**, 195 (1994); M. Lindberg, Y. Z. Hu, R. Binder, and S. W. Koch, Phys. Rev. B **50**, 18060 (1994).
[14] V. M. Axt and S. Mukamel, Rev. Mod. Phys. **70**, 145 (1998).
[15] S. T. Cundiff, M. Koch, W. H. Knox, J. Shah, and W. Stolz, Phys. Rev. Lett. **77**, 1107 (1996); M. U. Wehner, D. Steinbach, and M. Wegener, Phys. Rev. B **54**, R5211 (1996); D. Birkedal, V. G. Lyssenko, J. M. Hvam, and K. E. Sayed, *ibid.* **54**, R14250 (1996).
[16] C. N. Borca, T. Zhang, X. Li, and S. T. Cundiff, Chem. Phys. Lett. **416**, 311 (2005).
[17] X. Li, T. Zhang, C. N. Borca, and S. T. Cundiff, Phys. Rev. Lett. **96**, 057406 (2006).
[18] T. H. Zhang, I. Kuznetsova, T. Meier, X. C. Li, R. P. Mirin, P. Thomas, and S. T. Cundiff, Proc. Natl. Acad. Sci. U.S.A. **104**, 14227 (2007).
[19] L. Yang, I. V. Schweigert, S. T. Cundiff, and S. Mukamel, Phys. Rev. B **75**, 125302 (2007).
[20] I. Kuznetsova, P. Thomas, T. Meier, T. Zhang, X. Li, R. P. Mirin, and S. T. Cundiff, Solid State Commun. **142**, 154 (2007).
[21] M. Erementchouk, M. N. Leuenberger, and L. J. Sham, Phys. Rev. B **76**, 115307 (2007).
[22] W. Langbein and B. Patton, J. Phys.: Condens. Matter **19**, 295203 (2007).
[23] D. M. Dani, J. Tignon, M. Breit, D. S. Chemla, E. G. Kavousanaki, and I. E. Perakis, Phys. Rev. Lett. **97**, 057401 (2006).
[24] M. V. G. Dutt, J. Cheng, B. Li, X. D. Xu, X. Q. Li, P. R. Berman, D. G. Steel, A. S. Bracker, D. Gammon, S. E. Economou, R. B. Liu, and L. J. Sham, Phys. Rev. Lett. **94**, 227403 (2005).
[25] T. Brixner, J. Stenger, H. M. Vaswani, M. Cho, R. E. Blankenship, and G. R. Fleming, Nature (London) **434**, 625 (2005).
[26] M. O. Scully and M. S. Zubairy, *Quantum Optics* (Cambridge University Press, Cambridge, 1997).
[27] K. Leo, T. C. Damen, J. Shah, E. O. Göbel, and K. Köhler, Appl. Phys. Lett. **57**, 19 (1990).
[28] M. Joschko, M. Woerner, T. Elsaesser, E. Binder, T. Kuhn, R. Hey, H. Kostial, and K. Ploog, Phys. Rev. Lett. **78**, 737 (1997).
[29] K. B. Ferrio and D. G. Steel, Phys. Rev. Lett. **80**, 786 (1998).
[30] C. N. Borca, A. G. VanEngen Spivey, and S. T. Cundiff, Phys. Status Solidi B **238**, 521 (2003).
[31] I. Rumyantsev, N. H. Wong, R. Takayama, and R. Binder, Phys. Rev. B **65**, 245325 (2002).
[32] M. Phillips and H. Wang, Opt. Lett. **28**, 831 (2003).
[33] M. E. Donovan, A. Schülzgen, J. Lee, P.-A. Blanche, N. Peyghambarian, G. Khitrova, H. M. Gibbs, I. Rumyantsev, N. H. Kwong, R. Takayama, Z. S. Yang, and R. Binder, Phys. Rev. Lett. **87**, 237402 (2001).
[34] M. Koch, J. Feldmann, G. von Plessen, E. O. Göbel, P. Thomas, and K. Köhler, Phys. Rev. Lett. **69**, 3631 (1992).
[35] M. Koch, J. Feldmann, E. O. Göbel, P. Thomas, J. Shah, and K. Köhler, Phys. Rev. B **48**, 11480 (1993).
[36] A. Euteneuer, E. Finger, M. Hofmann, W. Stolz, T. Meier, P. Thomas, S. W. Koch, W. W. Rühle, R. Hey, and K. Ploog, Phys. Rev. Lett. **83**, 2073 (1999).
[37] S. T. Cundiff, Phys. Rev. A **49**, 3114 (1994).
[38] S. A. Hawkins, E. J. Gansen, M. J. Stevens, A. L. Smirl, I. Rumyantsev,

R. Takayama, N. H. Kwong, R. Binder, and D. G. Steel, Phys. Rev. B **68**, 035313 (2003).
[39] A. G. VanEngen Spivey, C. N. Borca, and S. T. Cundiff, Solid State Commun. **145**, 303 (2008).
[40] P. R. Berman and W. E. Lamb, Jr., Phys. Rev. A **2**, 2435 (1970).
[41] L. Yang and S. Mukamel, Phys. Rev. Lett. **100**, 057402 (2008).
[42] L. Lepetit, G. Chériaux, and M. Joffre, J. Opt. Soc. Am. B **12**, 2467 (1995).
[43] T. Zhang, X. Li, C. N. Borca, and S. T. Cundiff, Opt. Express **13**, 7432 (2005).
[44] C. Sieh, T. Meier, F. Jahnke, A. Knorr, S. W. Koch, P. Brick, M. Hübner, C. Ell, J. Prineas, G. Khitrova, and H. M. Gibbs, Phys. Rev. Lett. **82**, 3112 (1999); C. Sieh, T. Meier, A. Knorr, F. Jahnke, P. Thomas, and S. W. Koch, Eur. Phys. J. B **11**, 407 (1999).
[45] S. Weiser, T. Meier, J. Möbius, A. Euteneuer, E. J. Mayer, W. Stolz, M. Hofmann, W. W. Rühle, P. Thomas, and S. W. Koch, Phys. Rev. B **61**, 13088 (2000).
[46] L. Yang and S. Mukamel, J. Phys.: Condens. Matter **20**, 395202 (2008).
[47] T. Meier, S. W. Koch, M. Phillips, and H. Wang, Phys. Rev. B **62**, 12605 (2000).
[48] H. P. Wagner, W. Langbein, and J. M. Hvam, Phys. Rev. B **59**, 4584 (1999).
[49] F. Meier and B. P. Zakharchenya, *Modern Problems in Condensed Matter Sciences* (North-Holland, Amsterdam, 1984), Vol. 8.
[50] L. Yang and S. Mukamel, Phys. Rev. B **77**, 075335 (2008).